

Experimental characterization of the flowline of a lithium film formed using an electromagnetic thruster for a RAON prototype charge stripper

Authors: Kang, T., Lee, G., & Kim, H.R*.

Journal Information:

- **Journal:** Nuclear Engineering and Design
 - **Year:** 2023
 - **Volume:** 412
 - **Article ID:** 112481
 - **DOI:** <https://doi.org/10.1016/j.nucengdes.2023.112481>
-

ACCEPTED MANUSCRIPT NOTICE

© 2023. This manuscript version is made available under the CC-BY-NC-ND 4.0 license. (<http://creativecommons.org/licenses/by-nc-nd/4.0/>)

Disclaimer: This is a post-peer-review, pre-copyedit version of an article published in *Nuclear Engineering and Design*. The final authenticated version is available online at: <https://doi.org/10.1016/j.nucengdes.2023.112481>

Please cite the published version.

Experimental characterization of the flowline of a lithium film formed using an electromagnetic thruster for a RAON prototype charge stripper

Tae Uk Kang^{a§}, Geunhyeong Lee^{b§}, Hee Reyoun Kim^{a*}

§Lee and Kang contributed equally to this work

^a*Ulsan National Institute of Science and Technology, Department of Nuclear Engineering,
Ulsan 689-798, Republic of Korea*

^b*Korea Atomic Energy Research Institute,
111, Daedeok-daero 989 beon-gil, Yuseong-gu, Daejeon 34057, Republic of Korea
kimhr@unist.ac.kr

Short title: Analyzing a charge stripper using an electromagnetic thruster

Abstract

This paper describes the variable optimization of a lithium charge-stripper device and experimental characterization of lithium film formation for the charge removal of uranium using a magnetohydrodynamic liquid metal circulation system. To this end, liquid lithium thin films were developed using an electromagnetic thruster through collisions between a liquid lithium jet and a planar deflector. The lithium film flow characteristics were analyzed through simulation and waterjet experiments in terms of the liquid lithium film thickness. To circulate liquid lithium, a mechanically safe electromagnetic thruster with precise pressure control was designed by analyzing its electromagnetic and hydraulic parameters through finite element simulation. The analysis of the geometric arrangement of the permanent magnet and input current of the thruster revealed that compared to the existing electromagnetic thruster, the nominal input current of the newly-constructed one reduce by 57% and its weight reduced to 6%, and it required minimized input power, while facilitating maintenance. Further, the formation of a liquid lithium thin film with a thickness of 22 μm required to obtain the 79^+ charge state of uranium was verified at an input current of 107 A.

Keywords: Charge stripper; electromagnetic thruster; maintenance improvement; liquid-lithium film;

Nomenclatures

\vec{B}	Magnetic flux density [T]
B_t	Time-varying magnetic flux density [T]
B_r	r- direction magnetic flux density [A/m ²]
B_θ	θ - direction magnetic flux density [A/m ²]
B_z	z - direction magnetic flux density [A/m ²]
D	Hydraulic diameter [m]
d	Diameter [m]
E	Electric field [V/m]
E_t	Time-varying electric field [V/m]
E_p	electromotive force [n]
f	Force [N]
f_r	Friction factor
f_d	friction coefficient
f_d	Darcy friction coefficient of turbulent flow
H	Magnetic field intensity [A/m]
H_d	Height of the duct [m]
H_m	Magnetic field intensity of the permanent magnet [A/m]
i_{ver}	Current flowing [A]
i_p	Input current [A]
i_f	Fringing resistance [Ω]
J	Current density [A/m ²]
J_r	r- direction current density [A/m ²]
J_θ	θ - direction current density [A/m ²]
J_z	z - direction current density [A/m ²]
K_B	Total bend coefficient
K_l	Band resistance coefficient

L	Total length [m]
M	Magnetization [A/m]
n	Number of duct turns
R _f	Fringing resistance [Ω]
R _s	Resistance vertical to the current [Ω]
R _o	Outer resistance [Ω]
R _p	MHD circulator resistance [Ω]
R _{ver}	Vertical component resistance [Ω]
Re	Reynolds number
r	Duct radius (m)
t	Time [s]
v	Velocity [m/s]
W _d	Width [m]
ϵ_0	Electrical permittivity in vacuum [=8.85×10 ⁻¹² F/m]
ϵ_s	roughness height
ρ	Density [kg/m ³]
Δp_h	Hydraulic pressure loss [bar]
σ	Electrical conductivity [S/m]
μ_0	Magnetic permeability in vacuum [=4π×10 ⁻⁷ H/m]
μ_r	Relative magnetic permeability
χ_m	Magnetic susceptibility

1. Introduction

To obtain a certain amount of uranium energy (200 Mev/u), the charge removal of heavy ions is essential. A charge stripper is commonly used on a uranium beam with a charge state of 33^+ or 34^+ to increase the charge state to 79^+ [1,2]. To achieve a mean charge state of 79^+ , a liquid lithium thickness of $1.13 \times 10^{-3} \text{ g/cm}^2$ ($= 22 \mu\text{m}$) is required [2]. The efficiency of high-power heavy-ion accelerators can be enhanced using heavy-ion charge strips. Liquid lithium, which exhibits a large operating temperature range (melting point of 181°C , boiling point of 1342°C), low vapor pressure (10^{-7} Pa at 200°C) to minimize vapor pollution, low Prandtl number (~ 0.05), low thrusting power owing to its low density (513 kg/m^3), high heat capacity ($4.4 \times 10^{-3} \text{ J/kg} \cdot \text{K}$), and low viscosity [3] has been applied in the form of a thin film to remove the charge from uranium. Liquid lithium thin films are formed by the jet spray of liquid lithium thrust from the jet nozzle of an electromagnetic thruster. As shown in Figure 1, the electrons of the uranium beam are removed as the electrons flow from left to right in the liquid lithium thin film, thus changing the charge state of uranium from 34^+ to 79^+ [4].

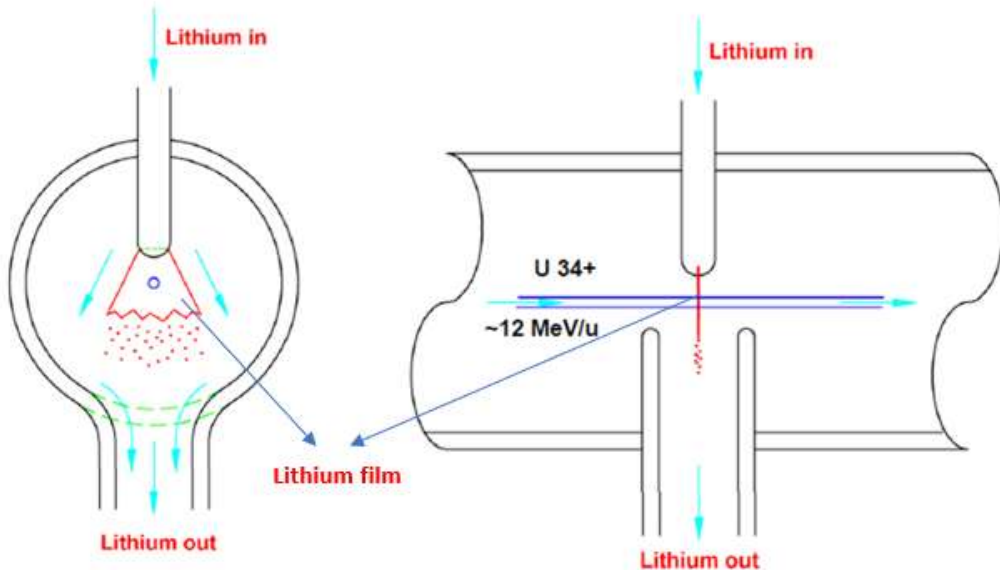


Fig 1. Charge removal process of a uranium ion passing through a liquid lithium film

Because liquid lithium is highly reactive with water and air, a non-contact electromagnetic thruster capable of generating electromagnetic force (Lorentz force) in liquid lithium is used for liquid lithium jet. Figure 2 shows that the electromagnetic thruster is physically enveloped by the external environment without an internal structure, such as an impeller or a sealing part [5]. The existing electromagnetic thruster shown in Figure 2 weighs 340 kg, which makes it difficult to maintain and manage; therefore, this study redesigned the electromagnetic thruster to reduce its weight. The

characteristics of the redesigned electromagnetic thruster are as follows. First, even if the magnetic field is not located in all directions (located only in one direction), there is no significant difference in the efficiency if the current only flows in the direction where the magnetic field is applied. By attaching a magnet to one direction of the duct, the magnetic field strength increases and the amount of ferromagnetic material required to shield the magnetic field considerably reduces, thus enabling the circulation of a small amount of liquid lithium. In addition, the redesigned structure increased the convenience of the maintenance process as the flow path is easy to replace. A direct current (DC) conduction-type electromagnetic thruster requires a high current but less voltage (<1 V); thus, even if the resistance of the electrode is large, copper corrosion can be prevented by replacing copper with SUS316. Additionally, the constituent material of the electromagnetic thruster coil and charge stripper system is SUS316, which is a non-reactive material in a lithium fluid flow environment (an alkali metal), thus enabling continual stable operation. The newly designed DC conduction helical-type magnetohydrodynamic (MHD) electromagnetic thruster was employed to generate a continuous liquid lithium film for a charge stripper prototype that is used in Rare isotope Accelerator complex for ON-line experiments (RAON), which decreases the amount of the power supply by minimizing the current [5]. The thickness characteristics of the film were experimentally analyzed based on the components of the thruster according to the change in the flow rate.

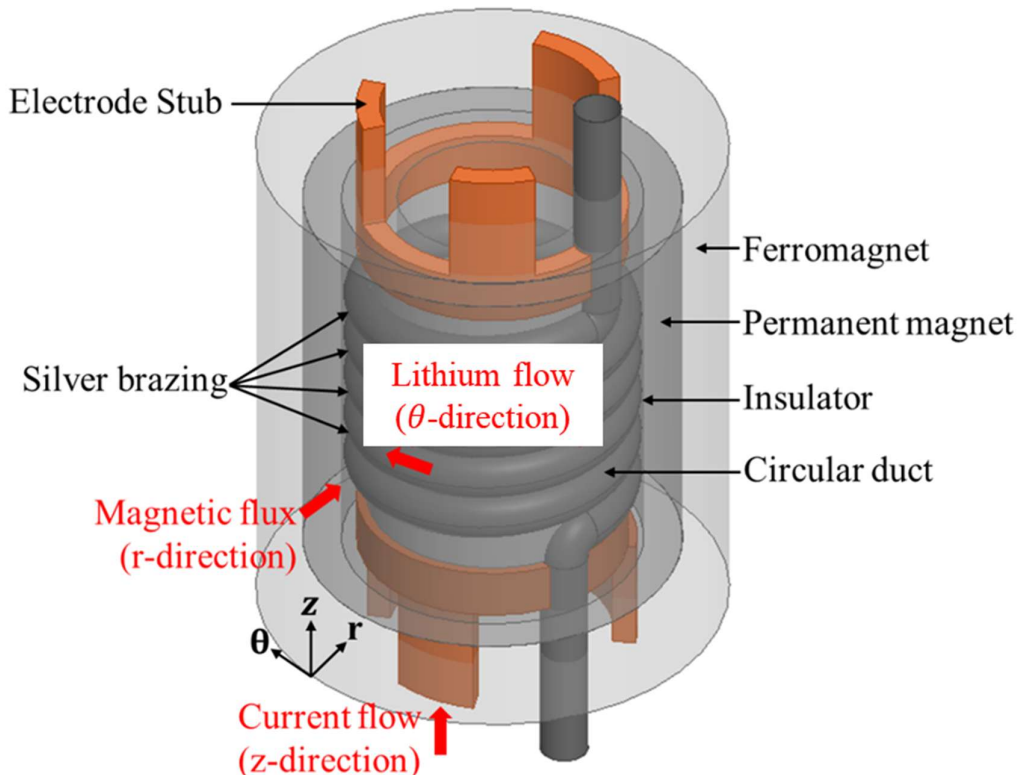


Fig 2. Design concept of the helical-type electromagnetic thruster

2. Methods

2.1. Theoretical approach for the design analysis of the helical-type electromagnetic thruster

The design variables were determined by solving MHD equations, including the electromagnetic and fluid equations. Ampere's law, Faraday's law, Gauss' law for magnetism, Ohm's law, and the fluid equation are expressed in Eqs. (1)–(4).

$$\text{Ampere's law: } \nabla \times \vec{B} = \mu_0(\vec{J} + \varepsilon_0 \frac{\partial \vec{E}}{\partial t}), \quad (1)$$

$$\text{Faraday's law: } \nabla \times \vec{E} = -\frac{\partial \vec{B}}{\partial t}, \quad (2)$$

$$\text{Gauss's law for magnetism: } \nabla \cdot \vec{B} = 0, \quad (3)$$

$$\text{Ohm's law: } \vec{J} = \sigma(\vec{E} + \vec{v} \times \vec{B}). \quad (4)$$

The magnetic field was simulated using ANSYS Maxwell. The boundary conditions were identical to those presented in Eqs. (5)–(9). The magnetic flux density in the flow path was analyzed using finite element method (FEM) by applying the permanent magnet's coercive force and the permeability of the ferromagnetic material. Magnetization (M) can be expressed as a relationship between the magnetic field strength (H) and the magnetic field strength of a permanent magnet (H_m) by considering both the permanent magnet and ferromagnetic material. This relationship can be expressed using Eq. (5):

$$\vec{M} = \chi_m \vec{H} + \vec{H}_m. \quad (5)$$

The overall magnetic flux density of the helical-type MHD electromagnetic thruster was calculated using Eq. (6), which considered the permanent and independent local magnetic fields, as well as the relative permeability:

$$\vec{B} = \mu_0(\vec{H} + \vec{M}) = \mu_0 \mu_r \vec{H} + \mu_0 \vec{H}_m. \quad (6)$$

The boundary conditions between the magnetic field intensity and magnetic flux density of materials of different permeabilities were determined using Eqs. (7)–(9):

$$\vec{H}_{t,1} = \vec{H}_{t,2}, \quad (7)$$

$$\vec{B}_{n,1} = \vec{B}_{n,2}, \quad (8)$$

$$\vec{H}_t|_{r=\infty} = 0. \quad (9)$$

This was simulated in COMSOL Multiphysics, and Eqs. (10)–(13) were used for this simulation. The force generated by the electromagnetic phenomenon was applied to the flow and solved through coupling:

$$\vec{J}_t = \sigma(\vec{E}_t + \vec{v} \times \vec{B}_t). \quad (10)$$

$$\vec{J}_t = J_r \hat{r} + J_\theta \hat{\theta} + J_z \hat{z}, \quad (11)$$

$$\sigma(\vec{E}_t + \vec{v} \times \vec{B}_t) = \sigma\{(E_r + v_\theta B_{i,z} + v_\theta B_{e,z})\hat{r} + (E_z - v_\theta B_{i,r} - v_\theta B_{e,r})\hat{z}\}, \quad (12)$$

$$J_r = \sigma(E_r + v_\theta B_{i,z} + v_\theta B_{e,z}), J_\theta = 0, J_z = \sigma(E_z - v_\theta B_{i,r} - v_\theta B_{e,r}). \quad (13)$$

The helical-type MHD system generated fluid velocity in a narrow channel through the Lorentz force, which only affects the fluid velocity in the θ direction, and is expressed using Eqs. (14)–(15) (also using Eq. (10)).

$$\begin{aligned} \vec{f} &= \vec{J} \times \vec{B} = \{\sigma E_\theta (B_{i,r} + B_{e,r}) - \sigma (v_\theta B_{i,z} - v_\theta B_{e,z})(B_{i,\theta} + B_{e,\theta})\}\hat{z} \\ &+ \{\sigma (E_z + v_\theta B_{i,r} + v_\theta B_{e,r})(B_{i,r} + B_{e,r}) - \sigma (v_\theta B_{i,z} + v_\theta B_{e,z})(B_{i,z} + B_{e,z})\}\hat{\theta} \\ &+ \{\sigma (E_z + v_\theta B_{i,r} + v_\theta B_{e,r})(B_{i,\theta} + B_{e,\theta}) - \sigma E_\theta (B_{i,z} + B_{e,z})\}\hat{r}, \end{aligned} \quad (14)$$

$$f_\theta = \sigma(E_z + v_\theta B_{i,r} + v_\theta B_{e,r})(B_{i,r} + B_{e,r}). \quad (15)$$

For an MHD transportation system with a high Hartmann number owing to the magnetic field, the Navier–Stokes equation can be expressed using Eq. (16), which can be reduced to Eq. (17) for a steady-state incompressible flow of liquid metal, where the viscosity term can be ignored [6]. Accordingly, the Navier–Stokes equation’s pressure gradient can be written as a number derived by multiplying the current density with the magnetic flux density.

$$\rho \left(\frac{\partial}{\partial t} + \vec{v} \cdot \nabla \right) \vec{v} = -\nabla p + \rho v \nabla^2 \vec{v} + \vec{J}_t \times \vec{B}, \quad (16)$$

$$\nabla p = \vec{J}_t \times \vec{B}. \quad (17)$$

The hydraulic pressure loss between the flow inlet and outlet was computed using the Darcy–Weisbach formula expressed in Eq. (18).

$$\Delta p_h = f_d \rho L v_\theta^2 / 2D + K_B \rho L v_\theta^2 / 2, \quad (18)$$

$$\frac{1}{\sqrt{f_d}} = -1.8 \log_{10} \left[\frac{6.9}{Re} + \left(\frac{\epsilon_s}{3.7D} \right)^{1.11} \right], \quad (19)$$

$$K_B = (n - 1)(0.25 \pi f_r r / d + 0.5 K_1) + K_1. \quad (20)$$

By considering the hydraulic pressure, as expressed in Eq. (15), the pressure developed between the flow inlet and outlet (Eq. (21)) can be derived by combining Eqs. (15)–(20):

$$\Delta p = 4 \int \{ \sigma (E_z + v_\theta B_{i,r} + v_\theta B_{e,r}) (B_{i,r} + B_{e,r}) \} dV / \pi d^2 - f_d \rho L v_\theta^2 / 2D - K_B \rho L v_\theta^2 / 2. \quad (21)$$

The coupling between electromagnetic and fluid effects was calculated using COMSOL Multiphysics code simulation. The input variables included material properties, input current, and initial fluid dynamic conditions, and the output variables included the developed pressure and electromagnetic field distribution.

2.2. Equivalent circuit equation

Figure 3 shows an illustration of the electric circuit methods for a helical-type MHD circulator. The force produced inside liquid lithium if affected by electromotive force (EMF) and the resistance of the thruster duct. To obtain the developed pressure in the liquid lithium of the thruster channel, equations for the helical-type MHD circulator were obtained using Kirchhoff's and Ohm's laws [7].

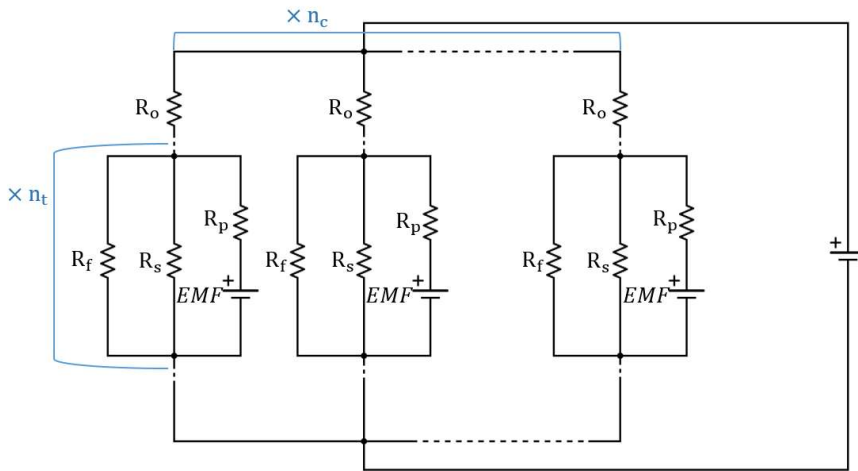


Fig 3. Equivalent circuit of a helical-type magnetohydrodynamic (MHD) circulator

When an electric current flows through an electrode into an MHD circulator, the current flows through the electrode.

Using Kirchhoff's law, the vertical component of the current flowing in the direction of the electrode stub and total input current can be represented as:

$$i_{ver} = i_f + i_s \quad (22)$$

$$i_t = i_p + i_{ver} \quad (23)$$

The resistance in the direction vertical to the current flow can be expressed as:

$$\frac{1}{R_{ver}} = \frac{1}{R_f} + \frac{1}{R_s} \quad (24)$$

Ohm's law can be used to determine the voltage based on the current path as:

$$R_o i_t + R_{ver} i_{ver} = R_o i_t + R_p i_p + E_p = V \quad (25)$$

According to the Lorentz principle, which follows an opposite trend to the generated force (voltage), the EMF interrupts the force generated (voltage) as follows:

$$E_p = BW_d v \quad (26)$$

The developed pressure was calculated by dividing the Lorentz force, which is the product of the magnetic flux density and current and width, by the flow area:

$$\Delta P_L = \frac{B}{H_d} i_p \quad (27)$$

The current flowing in the liquid lithium was obtained by combining Eqs. (28)–(31) and eliminating the outer resistance and vertical current flow:

$$i_p = \frac{R_{ver} i_t - BW_d v}{R_p + R_{ver}} \quad (28)$$

Additionally, the hydraulic pressure drop was calculated using the Darcy–Weisbach formula:

$$\Delta P_h = \frac{f_d \rho L v^2 (W_d + H_d)}{4 W_d H_d} \quad (29)$$

The friction coefficient can be expressed as a function of the Reynolds number, hydraulic diameter, and roughness height. [8,9]

$$f_d = \frac{64}{Re} \quad (30)$$

$$\frac{1}{\sqrt{f_d}} = -1.8 \log_{10} \left[\frac{6.9}{Re} + \left(\frac{\epsilon_s}{3.7D} \right)^{1.11} \right] \quad (31)$$

2.3. Helical-type electromagnetic thruster

The developed pressure was influenced by the multilayered duct geometry. Particularly, the permanent magnets and ferromagnetic materials in the θ direction did not dominantly affect the generated pressure. The geometries of the magnets and ducts were changed for maintenance (Figure 4) by reducing the overall weight of the thruster from 340 to 21 kg.

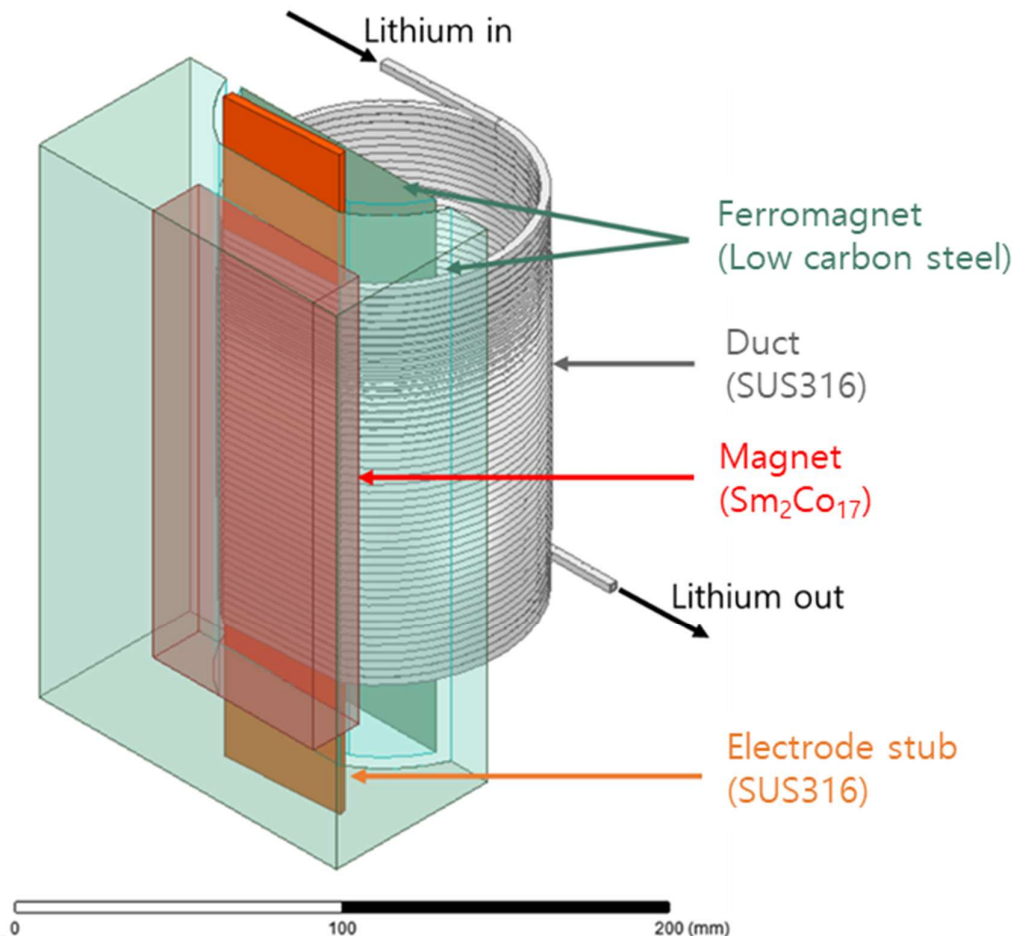


Fig 4. Conceptual design of the helical-type electromagnetic thruster

Figure 5 shows the shape of the MHD electromagnetic thruster used for the COMSOL simulation, in which the width, height, thickness, length, and number of turns were set as variables. The Lorentz force generated increased as the magnetic flux density increased, thereby reducing the required current. In addition, a ferromagnetic material, namely, ferromagnetic steel, was introduced to increase the magnetic flux density. Figure 6 shows the magnetic flux density according to the thickness of the ferromagnetic material. The thickness of ferromagnetic steel was set as 20 mm by considering maintenance issues—a further increase in thickness increased the weight, making duct maintenance difficult.

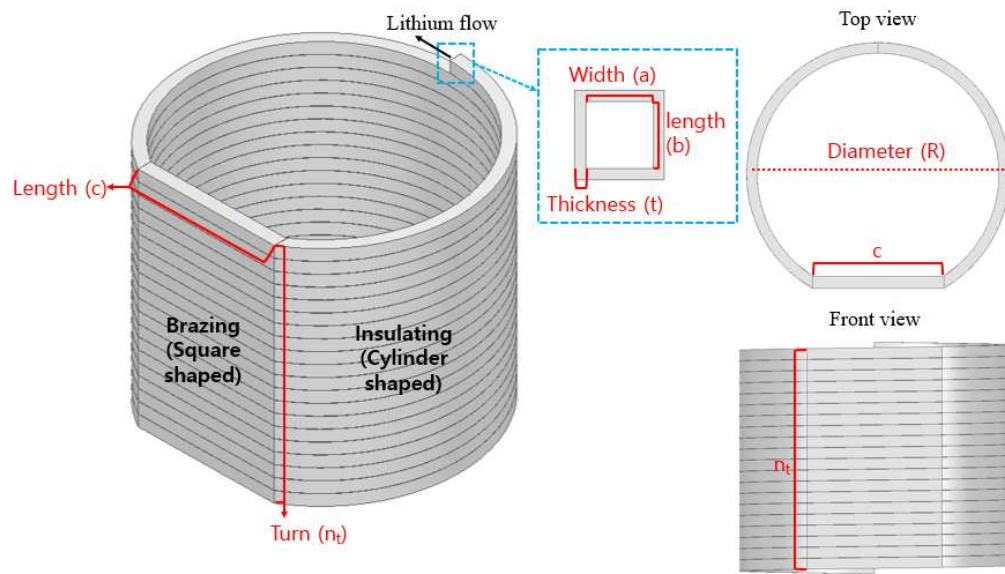


Fig 5. Geometry of the electromagnetic thruster used for the simulation

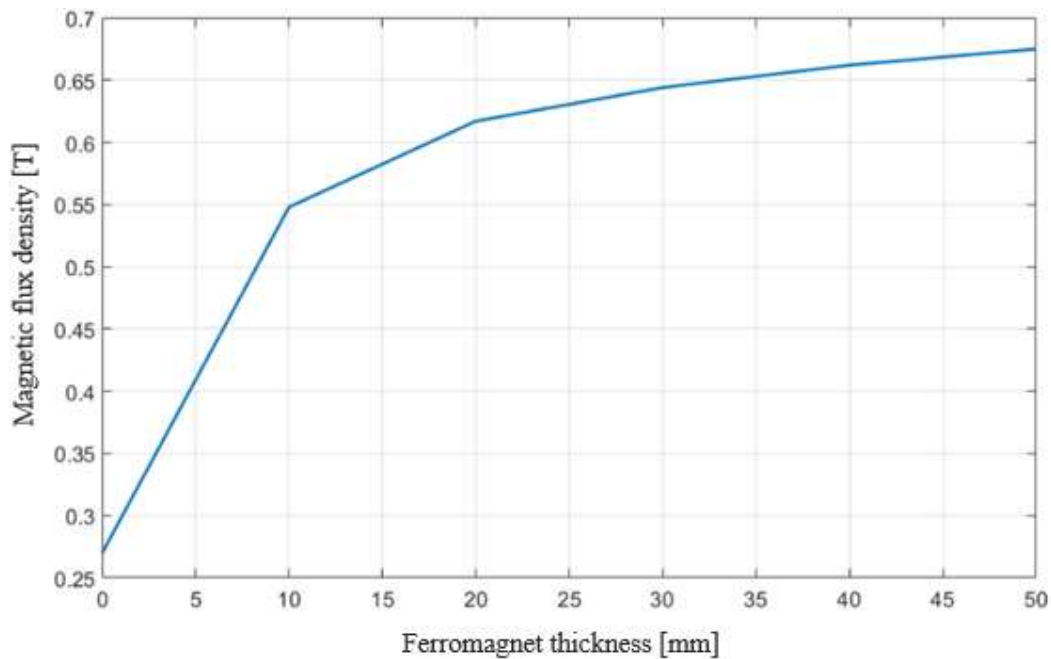


Fig 6. Magnetic flux density according to ferromagnet thickness
(width = 5 mm, height = 5 mm, thickness = 0.5 mm, and number of turns = 30)

As the number of turns in the duct increased, less current was required because the number of revolutions was equal to the number of times Lorentz force was applied. Figure 7 shows the relationship between the required current and number of turns. The number of rotations was determined as 30 by considering the duct productivity.

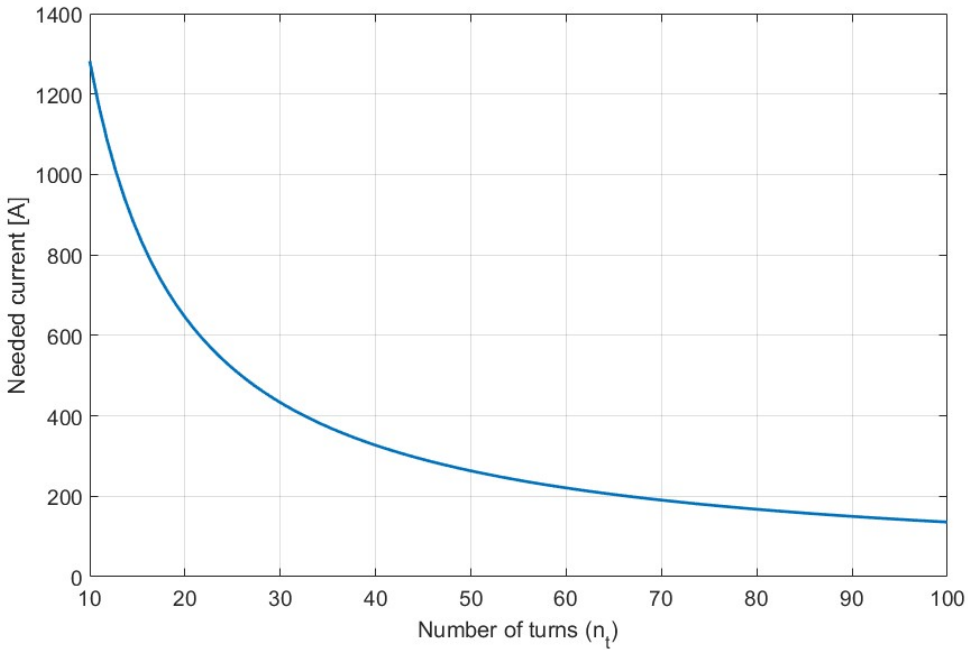


Fig 7. Needed current according to the number of turns
(width = 5 mm, height = 5 mm, and thickness = 0.5 mm)

Figure 8 shows the variation in the geometry of the MHD electromagnetic thruster. Increasing the duct width reduced the current required owing to the reduced hydraulic friction losses, and increased duct height, which increased the required current. A small duct height was created to prevent the clogging of the pipe with lithium oxide and to prevent the possibility of filling the thruster duct with steam that interferes with the current flow. Therefore, a 5-mm-height-long rectangular duct was adopted.

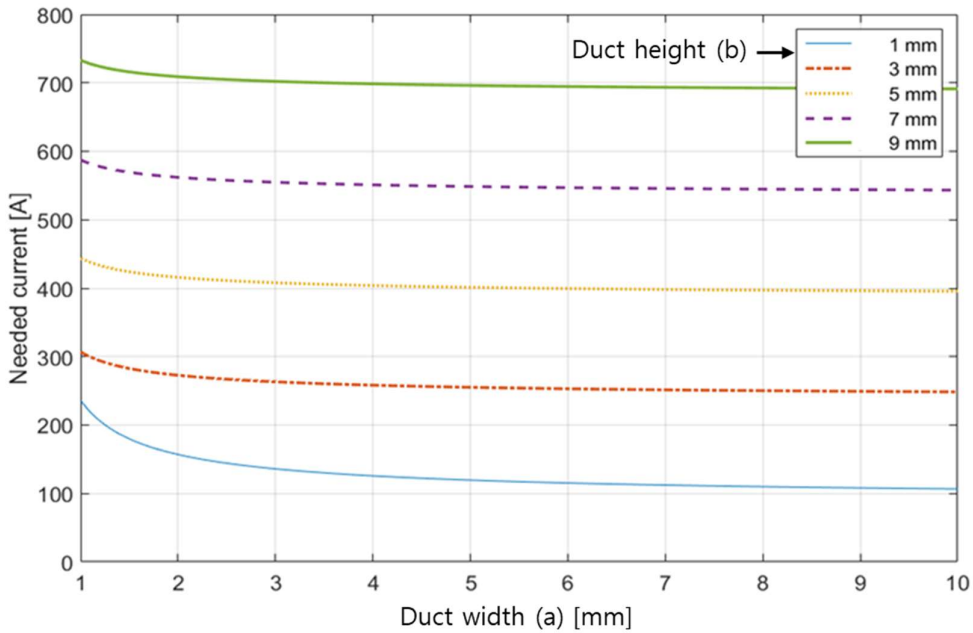


Fig 8. Needed current according to the height and width
(thickness = 0.5 mm and number of turns = 30)

When a ferromagnetic material was used in the magnet, the mean magnetic flux density of the MHD electromagnetic thruster was 0.6 T (Figure 9). The ferromagnetic material created a maximum magnetic flux density at the center. When an input current of 500 A was passed through the electromagnetic thruster, as shown in Figure 10, a pressure of 14.6 bar was generated. Each duct generated a pressure of approximately 0.5 bar.

Table 1 lists the design parameters of the new MHD electromagnetic thruster, and the P–Q curve characteristics of the corresponding thruster are shown in the Figure 11 [8]. The graph was optimized at approximately 6 cc/s. Compared to that of the existing design model, the total weight of the redesigned model was reduced to 6%. In addition, the input current was reduced from 872 to 500 A, and the generated pressure was 14% higher than that of the conventional units, even though the pressure increased from 10.5 to 14.6 bar. The light weight of the redesigned thruster will enable maintenance, and the newly designed MHD electromagnetic thruster could generate high-specification driving pressure at a lower current. In addition, the driving pressure of the new lightweight MHD electromagnetic thruster was 2.4 times greater than that of the existing one at the same input current [9].

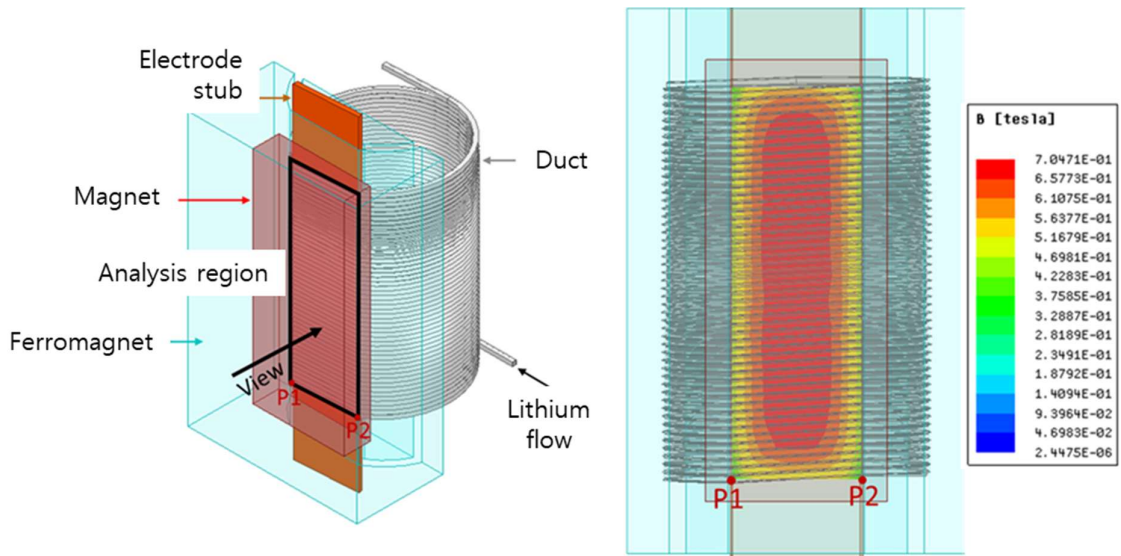


Fig 9. Magnetic flux density distribution of the electromagnetic thruster

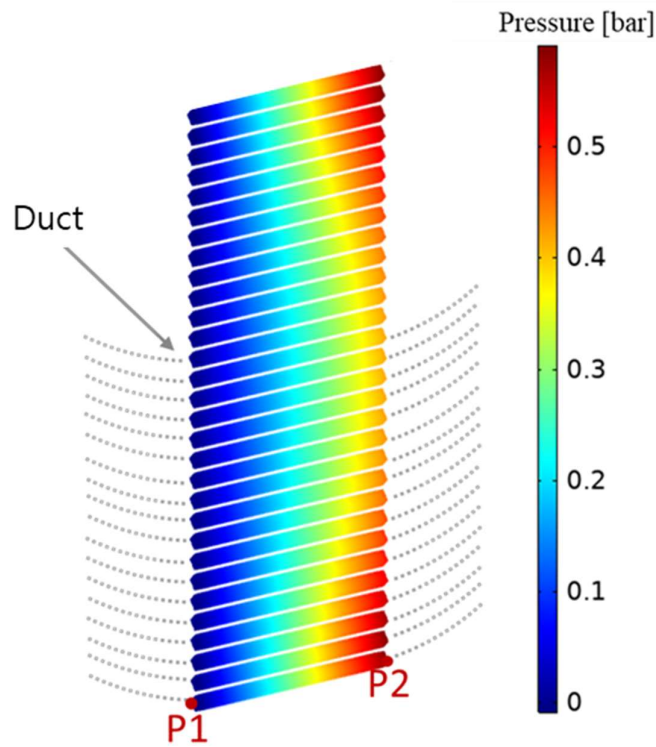


Fig 10. Generated pressure of each pipe section of the electromagnetic thruster

Table 1. Design variables of the electromagnetic thruster for FEM simulation

Variable	Units	Values
Flow rate	[cm ³ /s]	6
Developed pressure	[bar]	14.6
Temperature	[K]	473
Width and length of the flow channel (a,b)	[mm]	5
Thickness of the flow channel (t)	[mm]	0.5
Diameter of the flow channel (R)	[mm]	200
Length of electrode stub (c)	[mm]	50
Number of turns	-	30
Mean magnetic flux density	[T]	0.6
Input current	[A]	500
Weight	[kg]	21

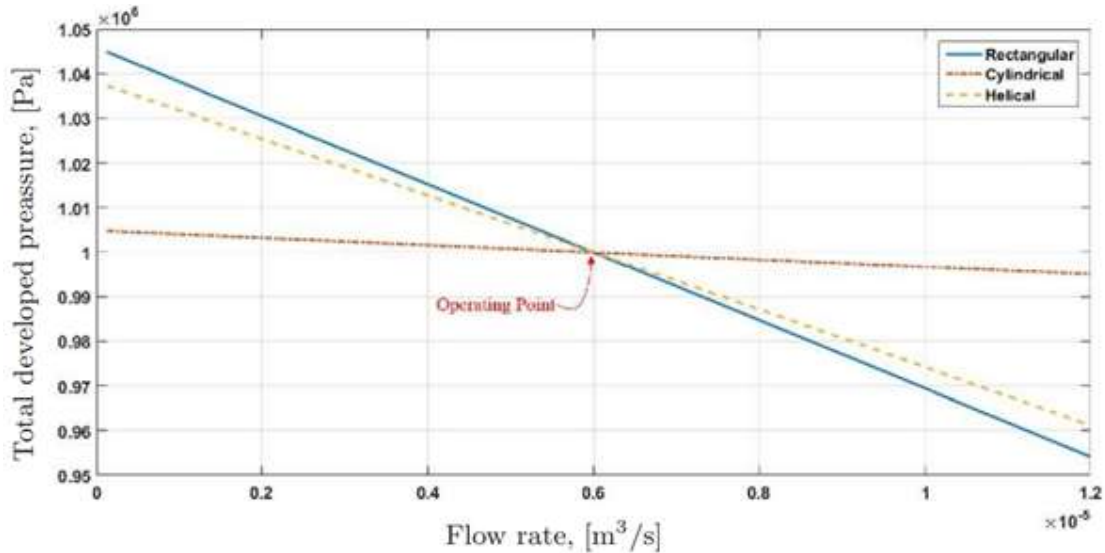


Fig 11. Developed pressure–flowrate curves of the three types of electromagnetic thruster

2.4 MHD electromagnetic thruster experimental setup (with thickness measurement)

Figure 12 shows the lithium-circulating system and its main components, namely, the lithium feed tank, lithium storage tank, MHD electromagnetic thruster, and charge stripper prototype. The lithium feed tank supplies lithium, and the lithium storage tank stores lithium when the system is not functional. The electromagnetic thruster installed in the circulation system was driven to drain liquid

lithium from a thin nozzle within the charge stripper prototype.

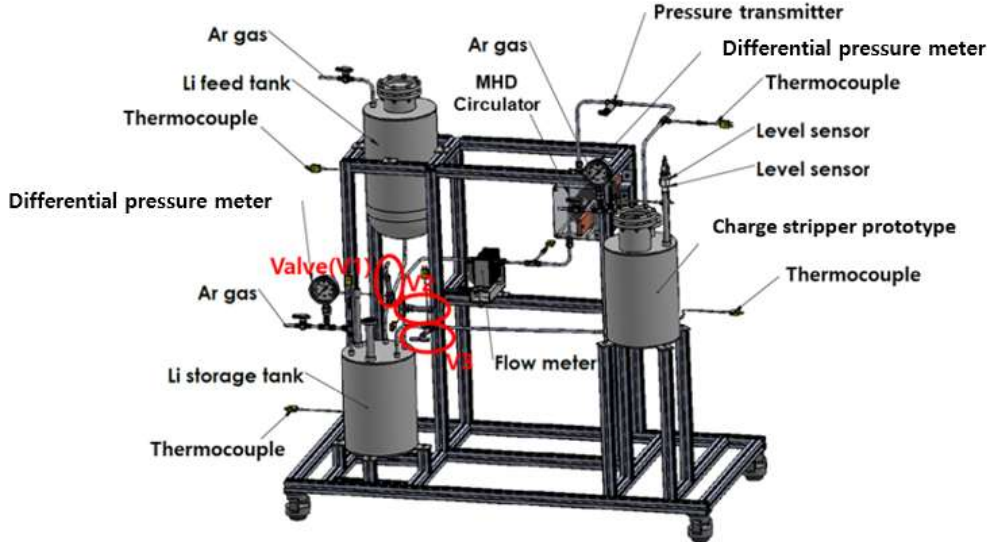


Fig 12. Electromagnetic thruster performance test loop system

2.6 Aluminum foil-based performance testing of the laser measurement system for the thickness measurement of the liquid lithium film

The existing technology uses an electron gun to measure the thickness of a lithium thin film; however, because an electron gun emits an electron beam, a radiation permit is required for its use [10]. Therefore, this study employed a laser measurement system (as shown in Figure 13). This system exhibits an alignment function, and the different wavelengths ejected from the laser were transmitted to the computer. The alignment was performed until the two lasers exhibited the same diffracted wavelengths location. Accordingly, the distance between the two devices could be determined using the reference specimen. After aligning, the distance between the two devices can be determined using the reference specimen. Two laser devices (Model CL-3000) were installed, and the thickness of the lithium thin film was measured by calculating the change in the laser transmission time with a change in the distance between the liquid lithium thin film and the laser device. In terms of specification, the resolution of the laser device was $2.5 \mu\text{m}$ and the distance that can be measured by a laser device was 120 to 160 mm. As only a short distance could be measured, the shape of the charge stripper prototype was changed, as shown in Figure 14.

The containment unit of the charge stripper prototype contained a viewport for observing the state of the liquid-lithium film. The deflector and nozzle influenced the formation of the liquid lithium film, and the level meter measured the flow rate of the electromagnetic thruster. The equivalent line functioned to equalize the pressure of the lithium film and storage tank, and the quartz view port was

used for visually observing the measurement performed by the laser device. Thickness calibration verification was performed (Figure 15) using 16-, 30-, 40-, and 50- μm aluminum foils, whose thicknesses were determined using the installed charge stripper prototype. Figure 15 reveals that the measurement errors at thicknesses of 16, 30, 40, and 50 μm were ± 1.5 , ± 2.5 , ± 2.5 , and $\pm 2.5 \mu\text{m}$, respectively, while the deviation interval of 2.5 μm satisfied the resolution of the laser thickness measurement system. In addition, the standard deviations at thicknesses of 16, 30, 40, and 50 μm were 1.29, 2.29, 1.84, and 1.29 μm , respectively, while the deviation interval of 2.5 μm satisfied the resolution of the laser thickness measurement system.

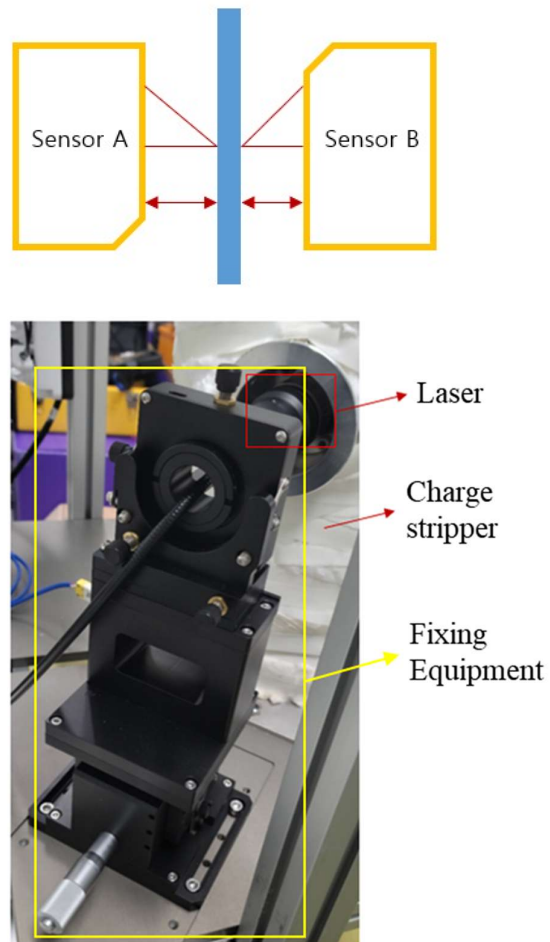


Fig 13. Laser measurement method

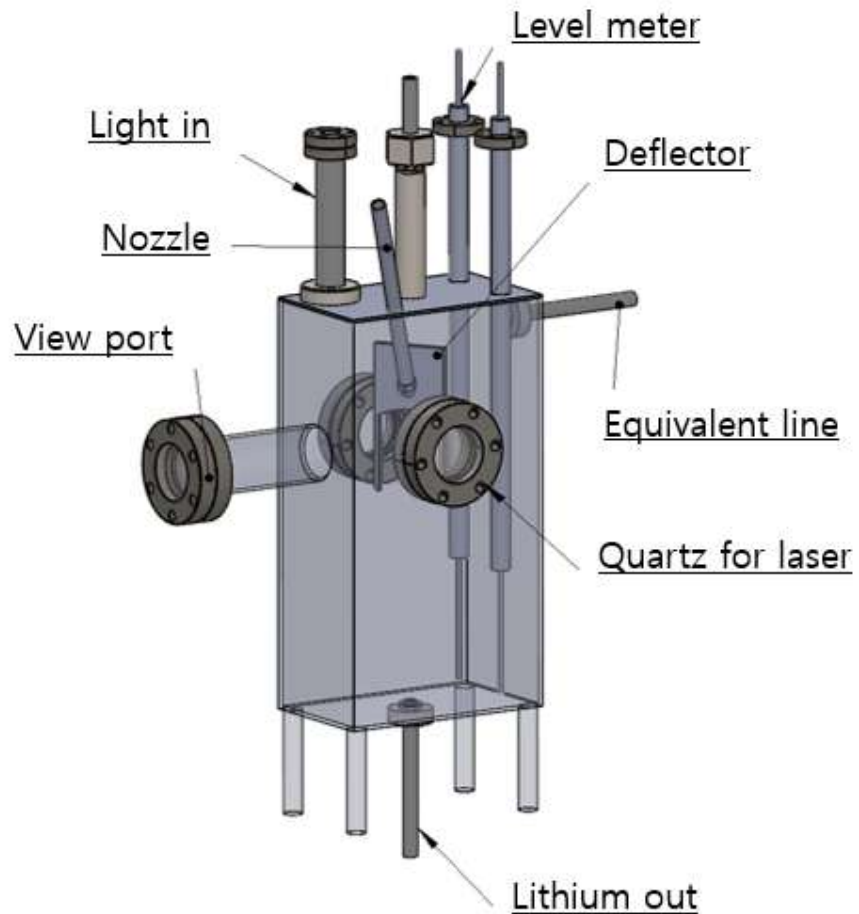


Fig 14. Design of the charge stripper prototype

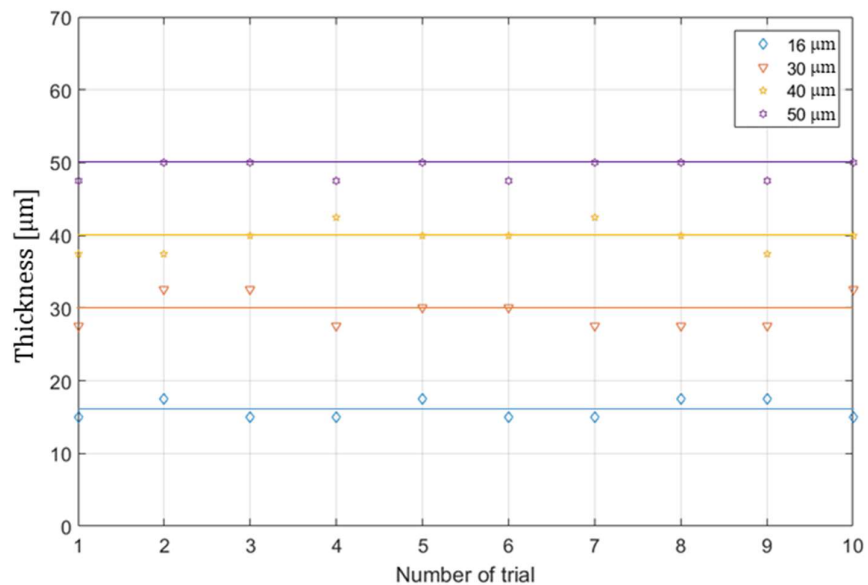


Fig 15. Thickness calibration

3. Results and discussion

3.1 Electromagnetic thruster

Figure 16 shows a schematic representation of the newly redesigned MHD electromagnetic thruster consisting of electrodes for supplying current, brackets for fixing, ducts, magnets, and a core. Copper electrodes cannot be employed for prolonged periods because they undergo rapid oxidation at high temperatures. Therefore, the electrodes used in this study were made of stainless steel (SUS316).

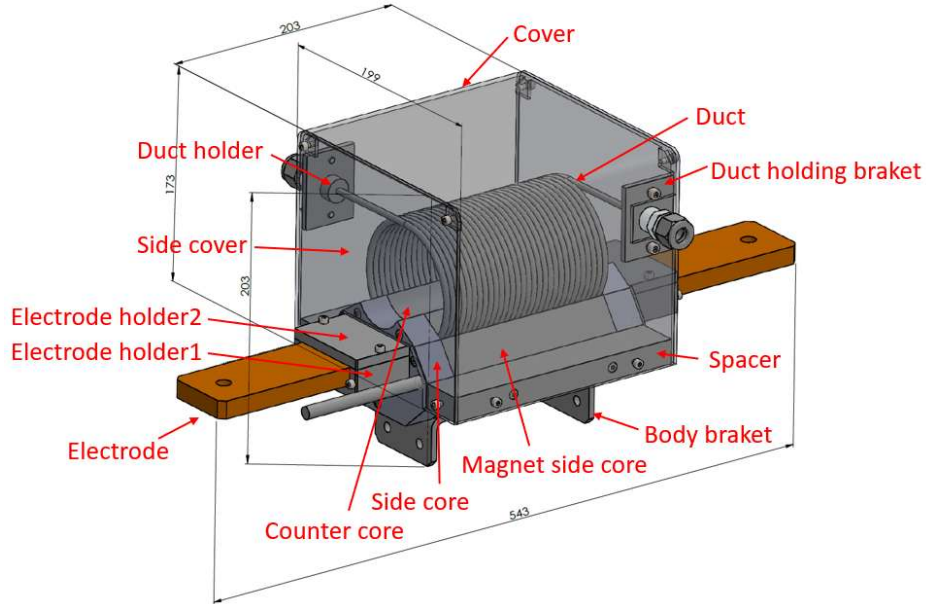


Fig 16. Diagram of the electromagnetic thruster

The fabrication of the new MHD electromagnetic thruster is shown in Figure 17. The reduction in the weight of the thruster from 340 to 21 kg for maintenance purposes facilitated the removal of the magnet core. Consequently, the flow path structure of the MHD electromagnetic thruster can be easily replaced in the case of an accident. The specifications of the power supply used in the MHD electromagnetic thruster are shown in the table 2.

Table. 2 Specification of power supply

	Value
Input voltage	380 V
Input current	30 A
Frequency	60 Hz
Output voltage	0–5 VDC
Output current	0–3000 A



Fig 17. Fabrication of the new electromagnetic thruster

The MHD electromagnetic thruster was successfully driven via a driving process, as shown in Figure 18. Several differential pressure gauges and flow meters were installed in the loop to enable precise measurement. The measured developed pressure and flow rate as a function of the current are presented in Table 3. Table 3 indicates that the developed pressure at 500 A was 8.95 bar, which was 0.62 times smaller than the simulation value (14.6 bar). This difference was attributed to the reduction in the magnetic flux density at a high temperature and fringing current from actual soldering.



Fig 18. Liquid lithium driving test

Table 3. Results of the liquid lithium electromagnetic thruster driving test

Current (A)	Developed pressure (bar)	Flow rate (cm ³ /s)
100	1.63	2.87 (± 0.02)
200	2.74	4.32 (± 0.04)
300	4.01	5.12 (± 0.06)
400	6.18	5.93 (± 0.07)

In this study, FEM simulations were performed to verify the water test and the thickness trend with a change in the flow rate, and the results are shown in Figure 19. The surface tension of liquid lithium is greater than that of water, and the difference in the Reynolds number of the two is approximately 1.2. The simulation results revealed that the thickness of lithium was 1.1 times higher than that of water. The results of the water simulation were consistent with the water experimental data.

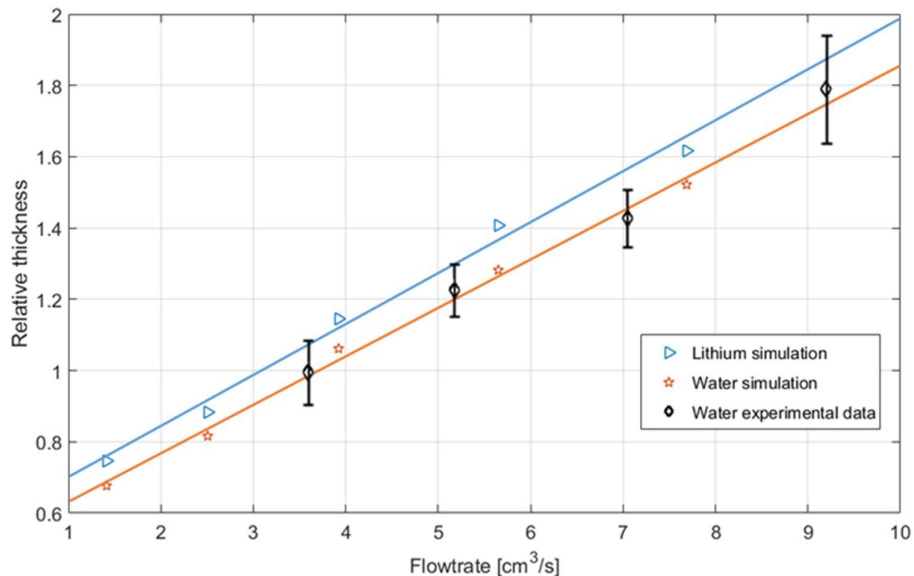


Fig 19. Finite element method (FEM) simulation analysis results of the water and lithium thickness

The nozzle angle was analyzed through the water experiments. As shown in Figure 20, the length of the resulting lithium film was stable between 30 and 38°, and the value did not appear linearly at angles beyond this, so the average nozzle angle was determined as 34°. To satisfy the 22 μm lithium film thickness, a nozzle with a minimum thickness of 0.7 mm was determined as ideal.

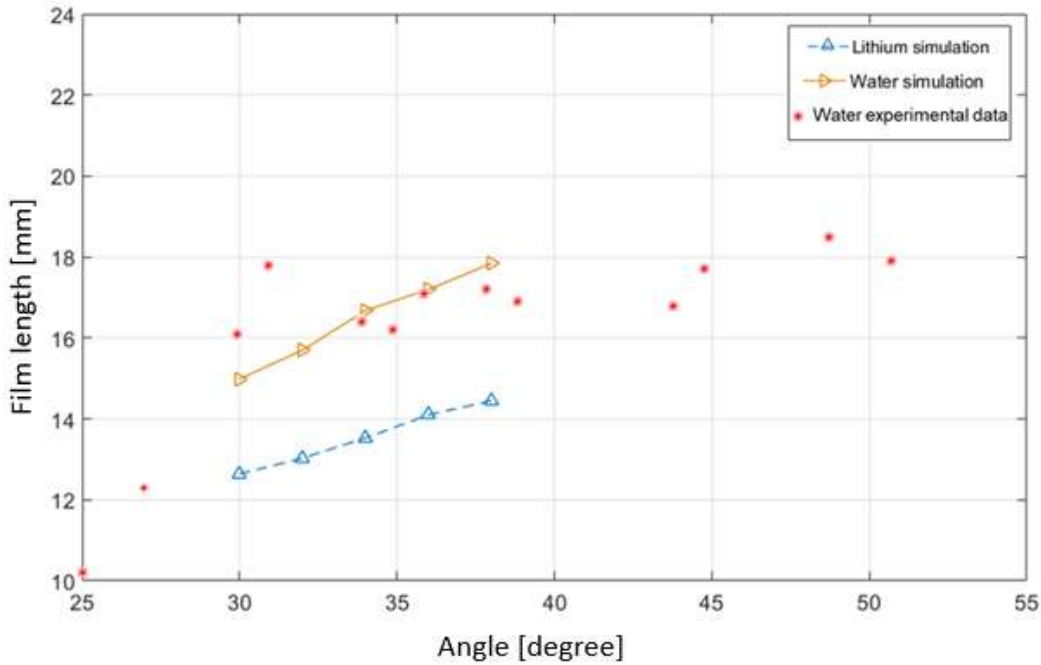


Fig 20. Change in film length as a function of the angle

The deflector was designed and constructed to determine the characteristics of the liquid thin film with a change in the shape of the deflector. Figures 21 (b) and (c) indicate that the respective deflector radii are set to 50 and 100, and do not have any significant impact on the shape of the film. However, the curvature of the deflector enabled the coalescence of the droplets. As the curvature increased, the deflector radius was set to 50 mm because of the decrease in the number of water droplets that can interfere with lithium film formation. The film thickness was less dependent on the geometry of the deflector.

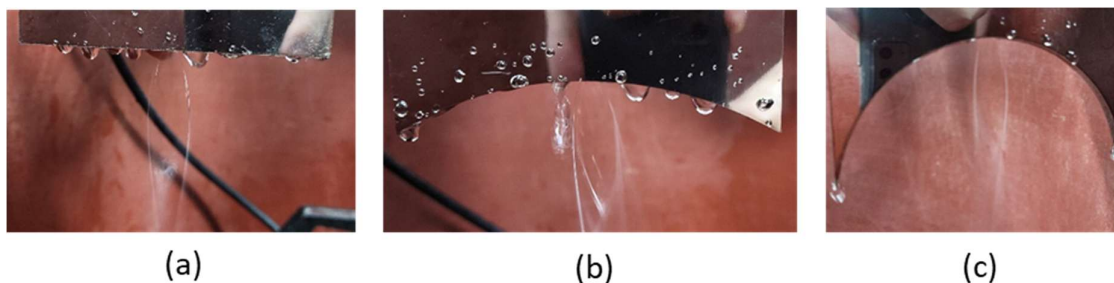


Fig 21. Deflector experiment: (a) flat, (b) R100, and (c) R50

Figure 22 shows the fabricated charge stripper prototype.



Fig 22. Fabricated charge stripper prototype

3.3. Experimental analysis of the liquid lithium film thickness

As shown in Figure 23, a liquid lithium film was successfully formed. The liquid lithium sprayed through the nozzle collided with the deflector to form a thin film. The thickness of the thin film was measured using a laser thickness gauge. The thickness and flow rate increased with an increase in the input current. The laser measuring device measures the thickness at the time when the laser is reflected. The shape of the lithium film became inflated owing to splashing liquid, and the bouncing off of lithium increased with an increase in the input current, resulting in an unstable shape. The thickness of the thin film based on the flow rate is shown in Figure 24.

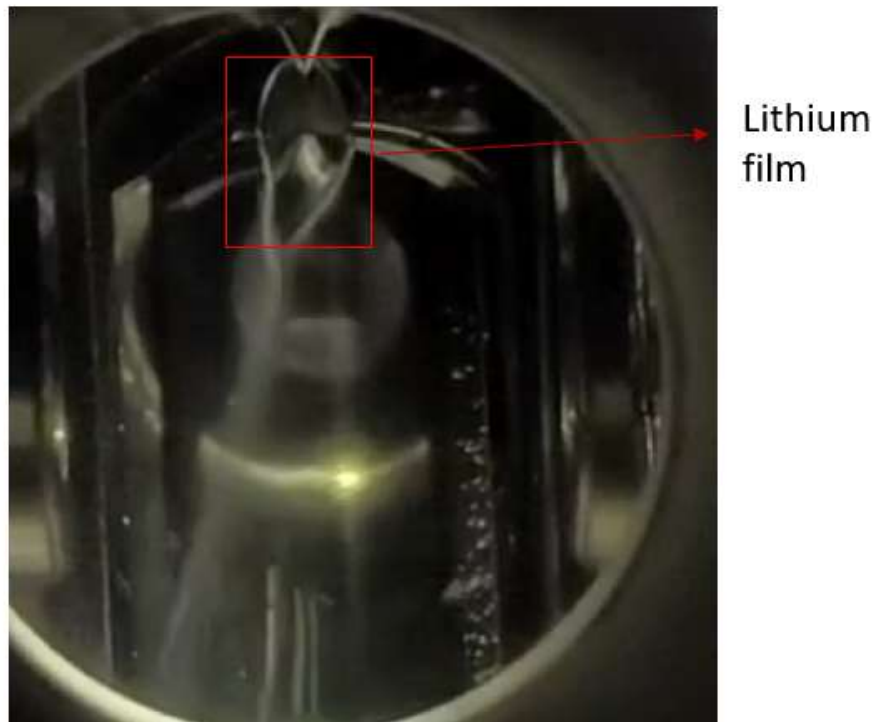


Fig 23. Liquid lithium film formation experiment

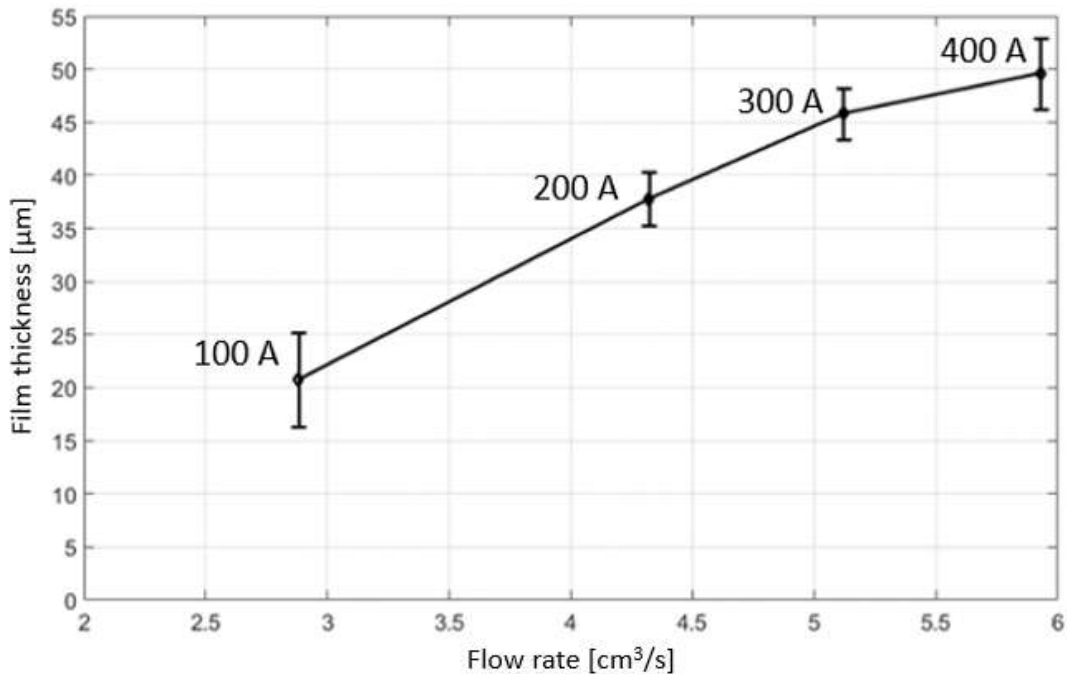


Fig 24. Liquid-lithium film thickness according to the flow rate

4. Conclusions

A lithium charge stripper prototype for removing uranium charge was optimally designed using an MHD liquid-lithium circulating electromagnetic thruster of which structure was optimized in a direction that was easy to maintain and its weight was greatly reduced. A new attempt by using a laser thickness measuring device was made for the measurement of the thickness of the lithium film and its thickness on the change of input current was experimentally verified.

The results revealed that the ideal nozzle diameter and angle that ensured stability and satisfied the lithium film thickness ($22 \mu\text{m}$) were 0.7 mm and 34° , respectively. The deflector was manufactured with a curvature that minimized the contamination problem of lithium droplets. The results confirmed that the flow rate and liquid lithium film thickness increased as the input current increased. In addition, the results confirmed that the liquid lithium thin film thickness of $22 \mu\text{m}$ could be achieved at an input current of 107 A .

This research provides experimental evidence for the fabrication of an MHD electromagnetic thruster-based charge stripper prototype. The optimized charge stripper prototype can be used to fabricate liquid lithium films for increasing the charge state of heavy-ion beams passing through it to obtain an energy of 200 MeV/u .

Acknowledgment

This work was supported by the Rare Isotope Science Project of the Institute for Basic Science funded by Ministry of Science and ICT and NRF of Republic of Korea (2013M7A1A1075764) and the Korea Institute of Energy Technology Evaluation and Planning and the Ministry of Trade, Industry & Energy (MOTIE) of the Republic of Korea (grant no. 20214000000410)

References

- [1] Rare Isotope Science Project (2012) *Baseline design summary*.
- [2] J. Song, Study of the interaction of charged ions with matter-development of charge stripper and IF production target at RISP, Doctoral dissertation, Seoul National University, 2016.
- [3] C.B. Reed, J.A. Nolen, J.R. Specht, V.J. Novick, Engineering and safety issues of lithium targets and film strippers. in: Proceedings of the Sixth International Meeting on Nuclear Applications of Accelerator Technology, 2016.
- [4] Y. Momozaki, J. Nolen, C. Reed, V. Novick, J. Specht, Development of a liquid lithium thin film for use as a heavy ion beam stripper, *J. Instrum.* 4(04), (2009) P04005.
- [5] G.H. Lee. H.R. Kim, Magnetohydrodynamics approach for active decay heat removal system in future generation IV reactor, *Int. J. Energy Res.* 42(10), (2018) 3266–3278.
- [6] M.S. Tillack, N.B. Morley Magnetohydrodynamics. McGraw-Hill, 1998.
- [7] B.K. Nashine, S.K. Dash, K. Gurumurthy, U. Kale, V.D. Sharma, R. Prabhakar, M. Rajan, G. Vaidyanathan, Performance testing of indigenously developed DC conduction pump for sodium cooled fast reactor, *Indian J. Eng. Mater. Sci.* 14, (2007) 209–214.
- [8] S.E. Haaland. Simple and explicit formulas for the friction factor in turbulent pipe flow, *J. Fluids Eng.* 105(1), (1983) 89–90.
- [9] G.H. Lee H.R. Kim, Numerical investigation and comparison of the rectangular, cylindrical, and helical-type DC electromagnetic pumps. *Magnetohydrodynamics* 53(2), (2017) 429–438.
- [10] S. Halfon, M. Paul, A. Arenshtam, D. Berkovits, D. Cohen, I. Eliyahu, D. Kijel, I. Mardor, I. Silverman, High-power electron beam tests of a liquid-lithium target and characterization study of ^{7}Li (p, n) near-threshold neutrons for accelerator-based boron neutron capture therapy, *Appl. Radiat. Isot.* 88, (2014) 238–242.